PAPER

Check for updates

Co-sputtered CuPt/Ag alloy nanoparticles and comparative catalytic performance of mono-, bi-, and tri-metallic nanoparticles in the oxygen reduction reaction†

Mingbei Zhu, Mai Thanh Nguyen, [iD] * Wei Jian Sim [iD] and Tetsu Yonezawa [iD] *

CuPt/Ag trimetallic alloy nanoparticles (NPs) were synthesized by co-sputtering onto liquid polyethylene glycol (PEG), using a CuPt alloy target and an Ag target. The fine structure analysis reveals that the obtained NPs are trimetallic solid solution alloys. Ag compositions increased with the increase of sputtering currents applied to an Ag target while keeping the sputtering currents applied to CuPt target constant. Moreover, it was found that the Cu : Pt atomic ratios of single NPs measured by energy dispersive spectroscopy (EDS) coupled with scanning transmission electron miscroscopy (STEM) were lower than the average value of the sputtered NPs dispersed in PEG. This suggests that NPs which are big enough to be checked by STEM-EDS are mainly Pt-rich NPs. The Cu, Ag, and Pt compositions of trimetallic NPs varied in a wide range, indicating random alloy formation. The sputtered trimetallic CuPt/Ag NPs were studied as catalysts in the oxygen reduction reaction (ORR), and the catalytic performance is compared with sputtered bimetallic alloy Cu/Pt and Ag/Pt NPs and monometallic Pt NPs. Trimetallic CuPt/Ag NPs showed higher ORR catalytic activities than bimetallic alloy Cu/Pt NPs owing to their better stability and dispersibility on the carbon support. However, the trimetallic alloy NPs performed worse than bimetallic Ag/Pt NPs and Pt NPs. This is caused by Cu oxidation and dissolution of Pt and Cu. Comparable ORR catalytic peformance of Ag/Pt NPs (40 atom% Ag) with Pt NPs is thought to come from the synergy between Pt and Ag in the bimetallic alloy.

Introduction

Pt nanoparticles (NPs) have attracted a lot of attention due to excellent performance in electrochemical applications.[1,2]

Division of Materials Science and Engineering, Faculty of Engineering, Hokkaido University, Kita 13 Nishi 8, Kita-ku, Sapporo, Hokkaido 060-8628, Japan.
E-mail: mai_nt@eng.hokudai.ac.jp, tetsu@eng.hokudai.ac.jp

† Electronic supplementary information (ESI) available: Size distribution of CuPt/Ag NPs sputtered onto PEG for 30 min; TEM image and size distribution of (CuPt)0Ag50; UV-Vis spectra of pure Pt, Ag and Cu NPs sputtered onto PEG with 50 mA sputtering current. TEM images and SAED results of the samples co-sputtered on the TEM grids for 10 min; Lattice spacing distribution of trimetallic NPs; STEM-mapping images of trimetallic co-sputtered Cu/Pt/Ag alloy NPs; composition distribution of sample (CuPt)50 sputtered onto PEG; LSV curves and K–L plots of NPs/C catalysts; electron transfer number and potential calculated from K–L plots; STEM-HAADF images of sample (CuPt)50/C before and after electrochemical tests; STEM-EDS area analysis spectrum of (CuPt)50Ag0/C after electrochemical test; STEM-HAADF images of sample (CuPt)50Ag30/C after electrochemical tests; EDS elemental line profiles of sample (CuPt)50Ag30/C before and after electrochemical tests; XPS spectra of sample Ag50Pt50/C before (a, b) and after (c, d) electrochemical tests: (a and c) Pt 4f; (b and d) Ag 3d. TEM image of commercial Pt/C reference catalyst; electrochemical test results of Pt50Ag50/C (a–c) and (CuPt)50Ag0 (d–f) in 1 M KOH: (a and d) CV curves, (b and e) LSV curves, and (c, f) K–L plots. See DOI: https://doi.org/10.1039/d2ma00688j

However, Pt is scarce and expensive. Fortunately, metallic alloys are widely applied as electrocatalysts and synthesized in a variety of ways.[2–8] Therefore, people have been working on alloying Pt with other cheaper metals and on more effective synthesis methods to avoid wastage of Pt.[9–13] Sputtering is a conventional physical technique for preparing thin films on solid substrates from the bulk targets under vacuum and dry conditions.[14–18] In 1999, Wagner and Günter proposed the preparation of Fe and Ag nanoparticles by sputtering onto an oil.[19] In 2006, Torimoto *et al.* obtained Au NPs by sputtering Au onto a capturing liquid such as an ionic liquid (IL).[20] These studies opened up a new route for the synthesis of metal NPs.[21–24] Various non or low volatile liquids such as ionic liquids, oils and liquid polymers can also be applied as capturing liquids.[18,25–27] Fluorescent metal clusters could also be obtained by sputtering with metal-coordinating ligands in a capturing liquid.[28–32] They also applied the method with single sputtering target containing two metals in alternative configuration to synthesize alloy nanoparticles with controllable composition in ILs.[24,33,34]

Co-sputtering simultaneously uses two or more metal targets to create metal alloy NPs.[34–36] This method does not require toxic chemical reductants and the alloy formation is

not limited by the difference in redox potentials of metals.[34–36] Furthermore, the metal compositions of the alloy NPs can be controlled more facilily and in a versatile way by adjusting the parameters such as the relative position of the liquid substrate with respect to the target, the applied sputtering powers and currents. König et al. obtained Au–Cu alloy NPs in ILs by co-sputtering wherein the particle composition varied with the position of the cavities containing ILs in the vacuum chamber.[35] Chauvin et al. co-sputtered Au and Cu targets by varying the electrical powers applied to the Cu target to obtain Au, Cu oxide, and Au/Cu alloy NPs in pentaerythritol ethoxylate.[37] We successfully synthesized bimetallic Ag/Au, Cu/Au, Cu/Pd, Pt/Au, and Ag/Pt solid solution alloy NPs with a tunable composition by co-sputtering onto liquid polyethylene glycol (PEG) and varying the sputtering currents applied to metal targets.[13,36,38–41] Besides, we also shed light on the formation mechanism of alloy NPs.[13] Synthesis of trimetallic alloy NPs by sputtering onto a liquid has been reported by Cai et al.[42] They prepared PdAu/Pt NPs by successively sputtering onto ionic liquid (IL) containing carbon nanotubes and applied PdAu/Pt on carbon nanotubes to the methanol oxidation reaction (MOR). Pt-based NPs also showed good catalytic performance for other reactions.[43,44] However, there is still no report about using co-sputtering onto liquid substrates to synthesize trimetallic alloy NPs, their structure, and catalytic applications, which is the focus of the present paper.

Cu is not a noble metal. Both Cu and Ag are much cheaper than Pt (as of September 30, 2022, Cu: 7.64 USD per Kg, referred from **https://markets.businessinsider.com/**; Pt: 28148 USD per Kg, Ag: 618 USD per Kg, referred from **https://www.kitco.com/fix/**). Alloying Pt with Ag and Cu can reduce the cost and the amount of Pt in the catalyst. Moreover, our previous works demonstrated that co-sputtered Ag/Pt and Cu/Pt NPs are solid solution alloys throughout the miscibility gaps and intermetallic compositions.[13,39] In addition, alloying Pt with a second metal can modify the electronic and geometric structures of NPs and enhance their catalytic performance. Pt has been successfully alloyed with noble metals such as Au and Pd, as well as 3d transition metals such as Mn, Fe, Ni, Co, and Cu, to create enhanced ORR electrocatalysts.[45–48] Wojcieszak reported their discovery of the synergetic effect of Au–Cu bimetallic catalysts, in which Cu can activate oxygen molecules.[49] And the excellent catalytic activity and stability of Pt/Ag alloy catalysts have also attracted much attention and been studied.[50–54] Thus, we can expect the formation of catalytically active Cu/Pt/Ag trimetallic solid solution alloy NPs by co-sputtering. PEG was chosen as the liquid substrate in the present study because it is cheap and does not strongly bind to the surface of NPs where electrochemical reactions occur. The latter is good in the sense that PEG can be washed away and does not block contacts between catalysts and electrolytes.[1]

In this paper, CuPt/Ag trimetallic solid solution alloy NPs were synthesized by co-sputtering using a CuPt alloy target (25 atom% Pt) and an Ag target. The alloy compositions were varied by adjusting the sputtering currents applied to the Ag target. The Cu to Pt ratios of the synthesized CuPt/Ag NPs were

found to be smaller than that of the CuPt target. The synthesized trimetallic alloy NPs were examined as catalysts for the oxygen reduction reaction (ORR) in an acidic electrolyte. Compared with the sputtered Pt NPs and co-sputtered Ag/Pt bimetallic alloy NPs, bimetallic alloy CuPt NPs and trimetallic alloy CuPt/Ag NPs showed worse ORR performance, that is, lower onset ORR potential and smaller electron transfer number. This is caused by the oxidation and dealloying of Cu as well as the dissolution of the catalysts.

Experimental section

Materials

PEG (M_W = 600, Junsei, Japan), CuPt alloy target (50 wt% of Pt and 50 wt% of Cu, 50 mm in diameter, 3 mm in thickness, Tanaka Precious Metals, Japan), Ag target (99.99%, 50 mm in diameter, Tanaka Precious Metals, Japan), and transmission electron microscopy (TEM) grids (Nisshin EM, Japan) were used for sputtering experiments. Vulcan XC 72 (Fuel Cell Earth), isopropyl alcohol (IPA, Junsei, Japan), Nafion™ perfluorinated resin solution (5 wt% in mixture of lower aliphatic alcohols and 45% water, Sigma-Aldrich, America), and Pt/C as the reference catalyst (5 wt% Pt loading, Wako, Japan) were used for the ORR catalytic test. Water was purified using an Organo Puric System (>18 MΩ cm).

Synthesis of CuPt/Ag alloy NPs

Before sputtering, PEG was stirred under vacuum at 650 rpm in a flask in an oil bath for 2 h to remove water and gases; the temperature of the oil bath was set at 90 °C. After that 10 mL of PEG was added to a Petri dish with a diameter of 60 mm. The Petri dish was then placed horizontally in the center of the sputtering vacuum chamber. A stirrer was placed in the Petri dish under the surface of PEG. In order to synthesize CuPt/Ag trimetallic alloy NPs, the CuPt alloy target and Ag target were co-sputtered. The elemental ratios of CuPt/Ag NPs were controlled by adjusting the sputtering currents applied to the Ag target (0–50 mA) while keeping the electrical current applied to CuPt target constant at 50 mA. When a glass slide was used as the substrate, it was placed in the center of the Petri dish. The center of the Petri dish was located at a distance of 110 mm from the two metal targets. PEG was stirred at 80 rpm. No stirring was carried out if glass slides were used. After several times of vacuum and purging with inert Ar to remove O_2, the pressure of the vacuum chamber was maintained at 2 Pa. Cooling ethanol of 4 °C was used for cooling the metal targets during sputtering. Before collecting the NPs, the metal targets were sputtered for 10 min to clean the surfaces. During cleaning, removable shutters were located in front of the metal targets and above the Petri dish to prevent contamination from falling onto the PEG. The sputtering time was 30 min for collecting NPs in PEG. The sputtering system was equipped with a thermocouple and a temperature-controlled system to maintain the substrate temperature at 30 °C. Samples are labeled as (CuPt)xAgy according to the sputtering currents, x

and y (mA), applied to the CuPt and Ag targets, respectively. For example, sample (CuPt)50Ag10 was obtained by co-sputtering CuPt target at 50 mA and Ag target at 10 mA.

Characterization

UV-Vis spectra were collected immediately after sputtering deposition using a JASCO V-630 spectrophotometer and a quartz cuvette with an optical path of 1 mm. The baseline was collected using an empty quartz cuvette. The size and shape of the NPs were analyzed using TEM (JEOL JEM-2000FX, 200 kV) and scanning TEM (STEM, JEOL JEM-ARM200F, 200 kV and FEI Titan3 G2 60–300, 300 kV). Samples for TEM and STEM analysis were prepared by immersing TEM grids into NPs/PEG dispersions for 10 s, then immediately immersing the grids into ethanol for at least 20 min to remove excess PEG, and finally drying in air at room temperature for a few minutes. The size distributions were collected from TEM and STEM images by measuring approximately 150 particles in at least three different regions of the grid using ImageJ software. The crystal structure of NPs was evaluated using STEM high-angle annular dark-field (HAADF) images. The samples sputtered on glass slides were analyzed by X-ray diffraction (XRD, Rigaku Mini Flex II, Cu Kα radiation, λ = 1.5418 Å, scanning speed of 0.5° min^{-1}). The X-ray diffraction intensities for all samples were plotted as a function of 2 theta. Area analysis using energy-dispersive X-ray spectroscopy (EDS) coupled with STEM (JEOL JEM-ARM200F) was carried out to verify the existence of CuPt/Ag alloy NPs and their compositions. The metal compositions of NPs/PEG dispersions and metal loading on carbon of the catalysts were obtained using an inductively coupled plasma-atomic emission spectroscopy system (ICP-OES, Shimadzu ICPE-9000). For preparing the samples, aqua regia or nitric acid was added to 1 mL of NPs/PEG dispersion or 10 mg catalyst powders. Aqua regia was used to prepare samples for measuring Pt and Cu, and nitric acid was used to prepare samples for measuring Ag. The mixtures were then kept for at least 30 min. After the metals were entirely dissolved, the mixtures were centrifuged, the precipitates were discarded, and the supernatants were diluted to 10 mL for ICP-OES measurements. The durability of the catalysts after electrochemical tests were analyzed by X-ray photoelectron spectroscopy (XPS, JEOL, JPS-9200, Mg Kα source). The catalysts before and after electrochemical tests were collected and XPS was performed using 20 eV pass energy, and scanned 300 times.

Electrocatalytic test

For the preparation of catalysts, carbon (Vulcan XC 72) was added to the sputtered NPs/PEG dispersions. After that acetone was added to the mixture and the mixture was sonicated. The sample was then centrifuged, the precipitate was washed with acetone, and the process was repeated two more times. Finally, the solid (NPs/C) was dried and used as catalysts. Catalyst inks were prepared by dispersing the dried NPs/C solids (3 mg) in solutions of pure water (0.6 mL), Nafion (0.15 mL), and IPA (2.25 mL). Before electrochemical tests, the catalyst ink (4 μL) was sonicated and dropcast onto a glassy carbon rotating disk electrode (RDE, 5 mm in diameter) using a pipette. Then the RDE was dried overnight.

The ORR electrochemical tests were performed in aqueous 0.1 M HClO$_4$ at 293 K using a three-electrode system. Ag/AgCl in saturated (sat.) KCl and Pt wire are the reference and counter electrodes, respectively. RDE with the catalyst film is the working electrode. Ar was bubbled (100 mL min^{-1}) in the electrolyte for 30 min to obtain an Ar sat. electrolyte. After cyclic voltammetry (CV) baseline was measured in the Ar sat. electrolyte, O$_2$ was bubbled (100 mL min^{-1}) in the electrolyte for 30 min to obtain an O$_2$ sat. electrolyte. The CV and linear sweep voltammetry (LSV) results in the O$_2$ sat. electrolyte were used to evaluate catalytic performance. CV was performed with a stationary electrode using a sweep rate of 10 mV s^{-1} from 1.1 to 0 V $vs.$ RHE. LSV was measured using the RDE rotating at various rotation speeds (400, 900, 1225, 1600, 2025, 2500, and 3600 rpm) and a sweep rate of 5 mV s^{-1}. CV and LSV measurements were carried out without bubbling of Ar or O$_2$ gas. Electron transfer numbers (n) were calculated from the LSV results using the Koutecký–Levich (K–L) plot and Levich equation (explained in the ESI†). All reported potentials in this paper are referred to the reversible hydrogen electrode (RHE).

Results and discussion

Morphology and crystal structure of the sputtered NPs

Fig. 1 shows the STEM-HAADF results of the co-sputtered samples. The NPs dispersed well in the PEG and no agglomeration was found in the images. The size distributions of the samples are presented in Fig. S1 (ESI†). The average particle sizes and the sputtering currents of all samples are listed in Table 1. The average particle diameters of samples (CuPt)50Ag0, (CuPt)50Ag10, (CuPt)50Ag20, (CuPt)50Ag30, (CuPt)50Ag40, and (CuPt)50Ag50 are 1.3 ± 0.3, 1.4 ± 0.4, 1.3 ± 0.3, 1.6 ± 0.5, 1.6 ± 0.4, and 1.9 ± 0.4 nm, respectively. In general, the particle sizes of CuPt/Ag increase with the increase of the sputtering current of Ag.

Fig. 2 shows the UV-Vis spectra of the CuPt/Ag samples. (CuPt)0Ag50 NPs (only Ag NPs, 2.8 ± 0.7 nm, Fig. S2, ESI†) have a surface plasmon absorption peak at ≈420 nm, which is the characteristic property of Ag NPs. Note that Ag NPs > 1 nm show plasmon absorbance at about 400 nm or more.[55,56] The UV-Vis spectra of pure Pt, Ag and Cu NPs sputtered onto PEG are shown in Fig. S3 (ESI†). There is an absorption shoulder at ~280 nm in the Pt spectrum. However, in the spectra of other CuPt/Ag samples (average particle size ≥ 1.3 ± 0.3 nm), this
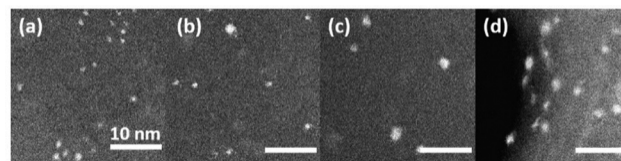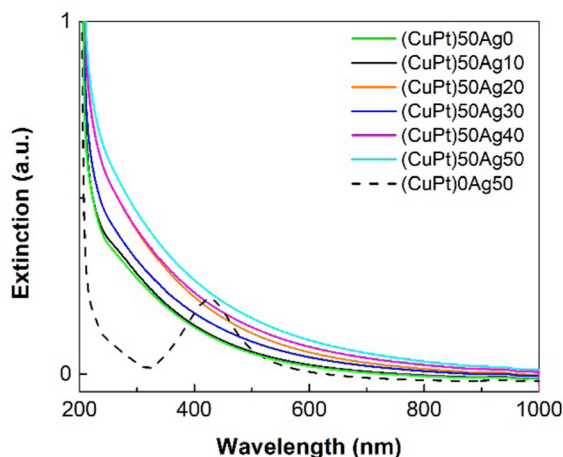

Fig. 1 STEM-HAADF images of the CuPt/Ag NPs sputtered onto PEG for 30 min: (a) (CuPt)50Ag0, (b) (CuPt)50Ag10, (c) (CuPt)50Ag30, and (d) (CuPt)50Ag50. All scale bars are 10 nm.
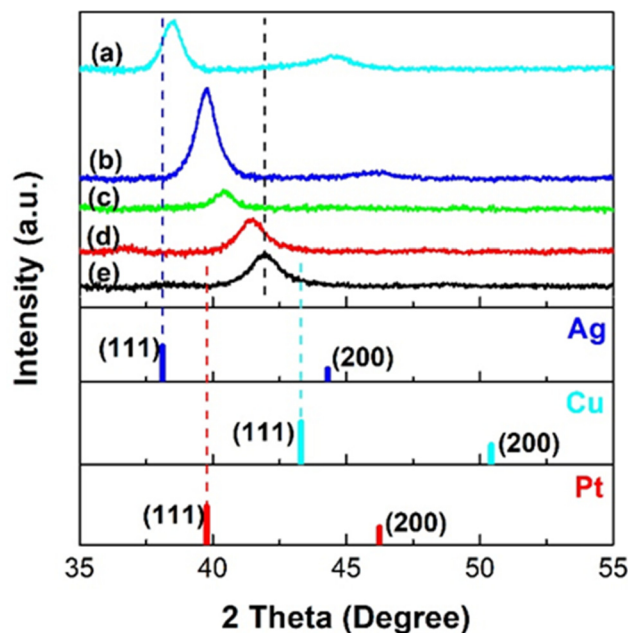
Table 1 Preparative conditions and sizes of CuPt/Ag NPs co-sputtered onto PEG

Sample	I_{CuPt} (mA)	I_{Ag} (mA)	Particle diameter measured by TEM/STEM (nm)
(CuPt)0Ag50	0	50	2.8 ± 0.7 (TEM)
(CuPt)50Ag0	50	0	1.3 ± 0.3 (STEM)
(CuPt)50Ag10	50	10	1.4 ± 0.4 (STEM)
(CuPt)50Ag20	50	20	1.3 ± 0.3 (TEM)
(CuPt)50Ag30	50	30	1.6 ± 0.5 (STEM)
(CuPt)50Ag40	50	40	1.6 ± 0.4 (TEM)
(CuPt)50Ag50	50	50	1.9 ± 0.4 (STEM)

Fig. 2 UV-Vis spectra of the co-sputtered (CuPt)50Ag0–50 and (CuPt)-0Ag50 NPs in PEG.

Fig. 3 XRD patterns of (a) (CuPt)0Ag50, (b) (CuPt)50Ag50, (c) (CuPt)-50Ag30, (d) (CuPt)50Ag10, and (e) (CuPt)50Ag0 samples synthesized by co-sputtering Ag and CuPt alloy targets onto glass slides for 10 min. Reference patterns (stick patterns) of Ag (JCPDF No. 01-087-0597, blue), Cu (JCPDF No. 00-004-0836, cyan), and Pt (JCPDF No. 00-004-0802, red) are shown at the bottom of the figure with the peak index.

typical peak of Ag NPs and absorption shoulder of Pt don't appear, indicating the formation of the CuPt/Ag alloy without pure Ag NPs. The extinction increases in the order of (CuPt)-50Ag0 < (CuPt)50Ag10 < (CuPt)50Ag30 < (CuPt)50Ag20 < (CuPt)50Ag40 < (CuPt)50Ag50. Thus, in general, the extinction of trimetallic CuPt/Ag NPs increases with the increase of sputtering currents applied to the Ag target, suggesting that the extinction is related to the presence of more Ag in the alloy NPs. However, despite the fact that (CuPt)50Ag30 is expected to have a higher Ag content than (CuPt)50Ag20, the extinction of (CuPt)50Ag30 is lower than that of the (CuPt)50Ag20 sample. The reason for this is not clear, further investigation is still needed. Possibly, the increase of extinction by having an Ag content in (CuPt)50Ag30 higher than that in the (CuPt)50Ag20 sample is compensated by larger particle sizes of (CuPt)50Ag30 (1.6 ± 0.5 nm) compared with (CuPt)50Ag20 (1.3 ± 0.3 nm). In particular, the (CuPt)50Ag20 sample has a higher number of small clusters (<1 nm) which contribute to increasing extinction.[25,57]

In order to analyze the crystal structure of the sputtered NPs using powder XRD, NPs should be separated from PEG. In general, the NPs/PEG dispersion was mixed with acetone and then centrifuged. However, because the co-sputtered CuPt/Ag NPs are small and stable in the PEG, they could not be separated from PEG by the mentioned method. Consequently,

the sputtering experiments on the glass slides to obtain aggregation of NPs/thin film with larger material quantities were carried out.

Fig. 3 shows the XRD patterns of the samples co-sputtered on the glass slides for 10 min. The (111) diffraction peak of sample (CuPt)50Ag0 is between the reference peaks of Pt and Cu, suggesting that it is a Cu/Pt solid solution alloy. The diffraction peaks of the trimetallic (CuPt)50Ag10–50 samples are between those of the samples (CuPt)50Ag0 and (CuPt)-0Ag50, which are CuPt alloy and Ag, respectively. Particularly, in the range between the (111) peaks of the reference Ag ($2\theta = 38.05°$) and the sputtered Cu/Pt alloy ($2\theta = 41.94°$, (CuPt)50Ag0 sample), each (CuPt)50Ag10–50 sample shows a single diffraction peak. Furthermore, as the sputtering currents applied to Ag target increase, the (111) peaks of the trimetallic samples shift towards that of Ag. These results suggest (CuPt)-50Ag10–50 samples are trimetallic solid solution alloy. From the (111) XRD peak broadening, crystallite sizes were calculated as 5, 7, and 11 nm for (CuPt)50Ag10, (CuPt)50Ag30, and (CuPt)50Ag50 samples, respectively. TEM image of the trimetallic samples sputtered on the TEM grids for 10 min (Fig. S4, ESI†) show that they have film-like structures of NPs with average particle sizes of 5.4 nm ((CuPt)50Ag10), 8.4 nm ((CuPt)50Ag30), and 9.7 nm ((CuPt)50Ag50). This agrees with crystallite sizes from the XRD result. The lattice spacings of the (111) planes of the trimetallic samples measured from SAED images (Fig. S4, ESI†) also increase with the increase of sputtering current applied to the Ag target, which corresponds to the increase of Ag composition. Ag has an atomic radius bigger

than Pt and Cu, hence, trimetallic alloy NPs with a higher Ag content show a larger lattice spacing. Therefore, the SAED result is consistent with the XRD results in showing the formation of solid solution alloy in CuPt/Ag NPs of sizes >5 nm. It is noted that the (111) peak of (CuPt)0Ag50 (sputtered Ag) in XRD pattern shifts to a higher angle compared with that of reference Ag. This is possibly caused by the lattice contraction of sputtered Ag with small size (Fig. S4, ESI†).[58]

The XRD, TEM, and SAED results of the samples sputtered on glass slides and TEM grids indicate that trimetallic alloy NPs (5–11 nm) were synthesized by co-sputtering. The sizes of trimetallic alloy NPs in the thin film on TEM grid/glass substrate (5–11 nm) are larger than trimetallic NPs synthesized in PEG (1.3–1.9 nm). It is known that atom diffusion and mixing to form alloy for small clusters/NPs are more facile than those for bigger particles. Hence, the small NPs sputtered onto PEG can be trimetallic alloys. In addition, as reported previously, the bimetallic alloy formed in the sputtering chamber before they grow on the solid surface or inside of PEG.[13] Therefore, with the formation of trimetallic alloy on glass slides and on TEM grids, we can expect trimetallic alloy formation when the substrate is liquid PEG. In order to check the fine structure and compositions of the NPs sputtered onto PEG, HAADF imaging and STEM-EDS were carried out and the results are discussed below.

Fine structure and composition of the sputtered NPs

Fine structure of the co-sputtered trimetallic NPs was analyzed with STEM-HAADF images (Fig. 4). Crystal structures of NPs were observed and the lattice spacings of (111) planes were 2.30, 2.32, and 2.35 Å for (CuPt)50Ag10, (CuPt)50Ag30, and (CuPt)50Ag50 NPs, respectively. The lattice spacings of the trimetallic NPs are between that of CuPt (2.29 Å, Fig. S4, ESI†) and Ag (2.36 Å, JCPDF No. 01-087-0597). The lattice spacing of each sample is distributed in a range (Fig. S5, ESI†). This is consistent with the fact that the composition of the sample is in a range (Fig. 5 and 6). In addition, overall lattice spacing distribution shift to higher value with the increase of the sputtering currents applied to Ag target. These results indicate the CuPt/Ag solid solution formation of a trimetallic alloy and is consistent with the XRD and SAED results of samples sputtered on solid substrates.

EDS elemental line profiles of samples (CuPt)50Ag10 and (CuPt)50Ag30 (Fig. 5) show that Cu, Pt, and Ag co-exist in single NPs. The STEM-EDS mapping results of samples (CuPt)50Ag10,
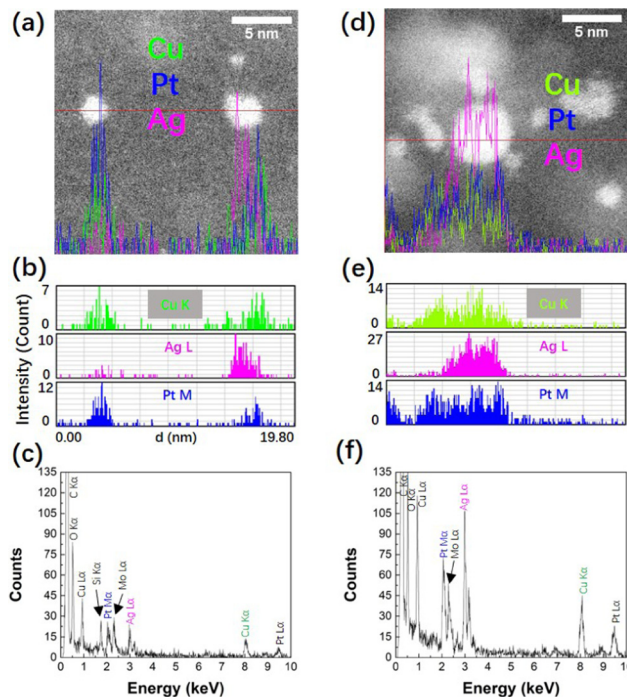

Fig. 5 EDS elemental line profiles of (a and b) (CuPt)50Ag10 and (d and e) (CuPt)50Ag30 NPs sputtered onto PEG at the positions marked by red lines crossing the NPs in (a and d) HAADF images. EDS spectra corresponding to the line profile of (c) (CuPt)50Ag10 NPs shown in (a and f) (CuPt)50Ag30 NPs shown in (d). Color code in line profile and EDS spectra: green, blue, and magenta are for Cu Kα, Pt Mα, and Ag Lα, respectively.

(CuPt)50Ag30, and (CuPt)50Ag50 are shown in Fig. S6 (ESI†). The co-presence of Cu, Pt, and Ag in the NPs was confirmed. Note that the line profile of some NPs (e.g., NP on the right of Fig. 5a) shows that Cu, Pt, and Ag elements do not exactly overlap in the same position). This suggests that phase segregation exists in some NPs and/or the trimetallic alloy composition in single NPs is not uniform.

The compositions of single CuPt/Ag trimetallic alloy NPs sputtered onto PEG were analyzed using STEM-EDS area analysis. The number of measured NPs is 59, 45, and 50 for (CuPt)50Ag10, (CuPt)50Ag30, and (CuPt)50Ag50, respectively. Atomic composition distributions and average compositions are shown in Fig. 6 and Table 2, respectively. The metal compositions distributed in a wide range, because the atoms combine with each other randomly in the sputtering chamber and PEG. As the sputtering currents applied to Ag target increase, the Ag atom% of single NPs increases. This accompanies with the decrease of Pt atom%.

However, the Cu atom% varies randomly among the samples. Moreover, the Cu contents (17 ± 15 atom% or less) are lower than Pt atom% (30 ± 20 atom% or more) with Cu : Pt of 0.46 : 1 (mol mol^{-1}) or less. These results are not expected because Cu and Pt were sputtered from a CuPt alloy target with higher Cu atom% than Pt atom% (75.4 atom% Cu, 24.6 atom% Pt, and Cu : Pt = 3.07 : 1 (mol mol^{-1})). Previously, we obtained a sputtered CuPt alloy with composition close to that of the CuPt target (76 atom% Cu) using a single head target sputtering onto
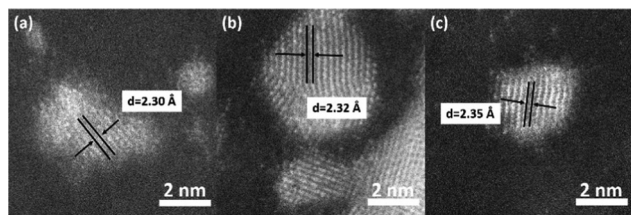

Fig. 4 HAADF images of (a) (CuPt)50Ag10, (b) (CuPt)50Ag30, and (c) (CuPt)50Ag50 NPs and the lattice spacing values of (111) planes.
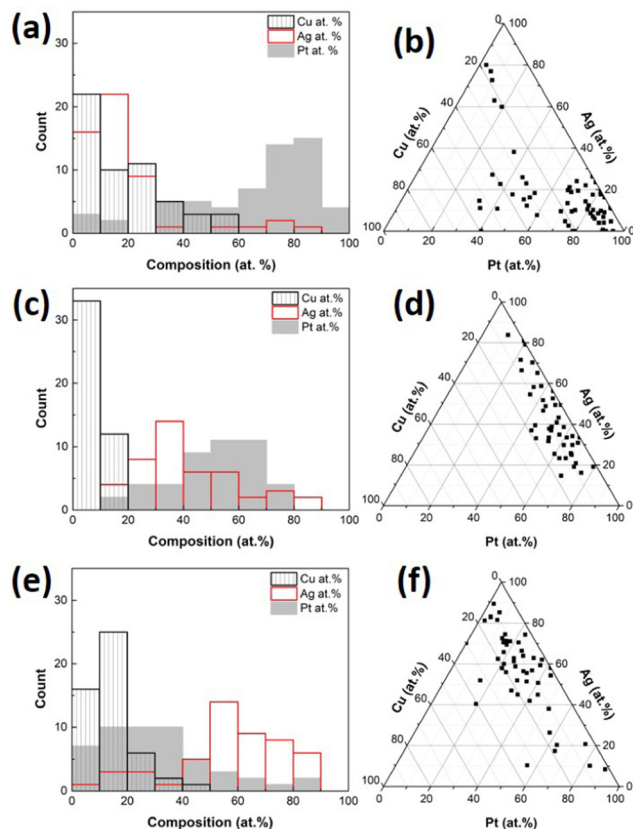
Fig. 6 Composition distributions of the co-sputtered CuPt/Ag samples: (a and b) (CuPt)50Ag10, (c and d) (CuPt)50Ag30, and (e and f) (CuPt)50Ag50. Each data point in the scatter plot of (b, d and f) represents the composition of a single NP measured by STEM-EDS and their locations in the triangular coordinate system represents the Cu, Pt, and Ag atom% of the NP.

glass for 30 min (70 atom% Cu as measured by XRF), on TEM grids for 30 s (72–76 atom% as measured by TEM-EDS), and onto PEG for 30 min (71 atom% Cu as inferred from lattice spacing from the high resolution-TEM image of CuPt NPs of 2.2 ± 0.6 nm).[39] Note that the NPs which could be analyzed using STEM-EDS area analysis with accuracy in the present study are ≈ 0.8 nm or more. Thus, we suspected that the Cu composition of NPs measured in the present study could be

affected by the limitation in the STEM-EDS analysis for small NPs (low signal and particle decomposition during observation) and the non-uniformity of the composition among single NPs in the samples. To verify this hypothesis, the composition of (CuPt)50Ag0 NPs of 1.3 ± 0.3 nm, which were sputtered using only the CuPt alloy target in the double head sputtering system, was also measured. The sample has an average 13 ± 9 atom% Cu and 87 ± 9 atom% Pt (Table 2 and Fig. S7, ESI†), which also shows lower Cu atom% than that of the alloy target. This confirms that the CuPt NPs measured using STEM-EDS with a particles size of about 1.3 nm are Pt-rich. Small NPs of below ≈ 0.8 nm could have higher Cu content but could not be measured in STEM-EDS area analysis. We could not rule out a possibility that not all the sputtered Cu formed trimetallic alloy with Pt and Ag. In addition, to confirm the existence of Cu and/or Cu-rich trimetallic NPs in PEG dispersion, the average compositions of all sputtered NPs in PEG dispersion were measured using ICP-OES. The ICP results (Table 2) show that with the increase of the sputtering currents applied to the Ag target, both Pt and Cu compositions decreased whereas Ag compositions increased as expected. Nevertheless, the ratios of Cu : Pt = 2 : 1 (mol mol^{-1}) remains similar in all the CuPt/Ag trimetallic samples and similar to that of the sputtered bimetallic Cu/Pt NPs obtained from only the CuPt alloy target. This reflects the fact that the Cu : Pt molar ratio in the co-sputtered NPs/PEG dispersions is fixed as expected. This ratio is smaller than the Cu : Pt molar ratio of the CuPt target (Cu : Pt = 3.07 : 1 (mol mol^{-1})), further research is essential for understanding of this phenomenon.

Catalytic performance

The co-sputtered (CuPt)50Ag30 NPs were loaded onto carbon as the support, henceforth labeled as (CuPt)50Ag30/C, for examining their ORR catalytic performance. The performance of CuPt/Ag trimetallic alloy NPs was compared with that of sputtered mono- (Pt) and bi-metallic ((CuPt)50Ag0 and Pt/Ag) NPs. Pt NPs (Pt50) were produced by sputtering of a Pt target onto PEG whereas Ag/Pt NPs (Ag50Pt50) were produced by co-sputtering of Ag and Pt targets onto PEG. Both samples were obtained using a double-target head system with sputtering currents applied to metal target of 50 mA. Fig. 7 shows the STEM-HAADF images of the catalysts on carbon. Except for Ag50Pt50

Table 2 Average compositions of co-sputtered CuPt/Ag samples in PEG

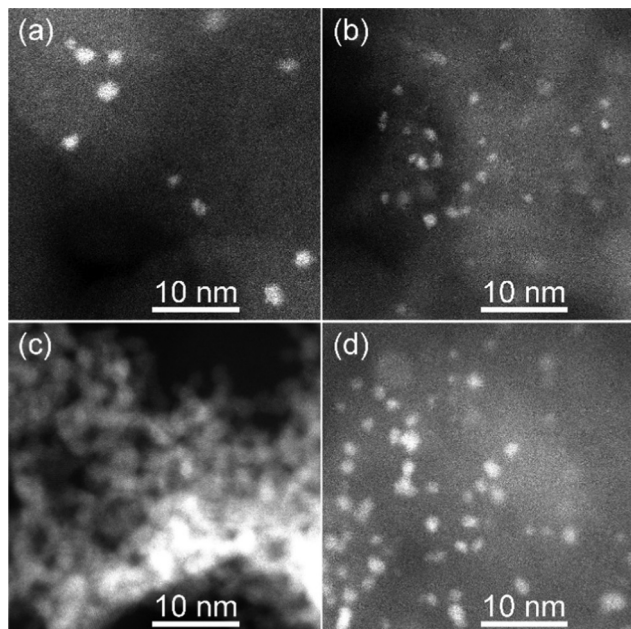| Composition		Samples			
		(CuPt)50Ag0	(CuPt)50Ag10	(CuPt)50Ag30	(CuPt)50Ag50
STEM-EDS	Cu (atom%)	13 ± 9	17 ± 15	7 ± 5	14 ± 8
	Pt (atom%)	87 ± 9	65 ± 24	51 ± 16	30 ± 20
	Ag (atom%)	0	18 ± 18	42 ± 18	56 ± 20
	Cu : Pt (mol mol^{-1})	**0.16 : 1**	**0.29 : 1**	**0.15 : 1**	**0.46 : 1**
	Ag : Pt (mol mol^{-1})	**0 : 1**	**0.30 : 1**	**0.83 : 1**	**1.9 : 1**
ICP-OES	Cu (atom%)	67.7	63.5	52.2	42.5
	Pt (atom%)	32.3	30.3	24.8	21.2
	Ag (atom%)	0	6.2	23	36.3
	Cu : Pt (mol mol^{-1})	**2.09 : 1**	**2.09 : 1**	**2.10 : 1**	**2.01 : 1**
	Ag : Pt (mol mol^{-1})	**0 : 1**	**0.20 : 1**	**0.93 : 1**	**1.72 : 1**

Fig. 7 STEM-HAADF images of the sputtered NPs after loading onto carbon for (a) (CuPt)50Ag30/C, (b) (CuPt)50Ag0/C, (c) Ag50Pt50/C, and (d) Pt50/C catalysts.

Fig. 8 (a) CV curves of (CuPt)50Ag30/C (blue), (CuPt)50Ag0/C (magenta), Ag50Pt50/C (green), Pt50/C (orange), and Pt/C reference (red) catalysts. (b) Enlarged part from 0 to 1.2 V of CV curves in (a). (c) LSV curves at different rotation speeds and (d) K–L plot from results in (c) of the (CuPt)50Ag30/C catalyst for calculating the electron transfer number.

NPs which appeared aggregated on carbon (Fig. 7c), the other catalysts have NPs well dispersed on carbon (Fig. 7a, b and d). Besides NPs, some atoms and small clusters of (CuPt)50Ag30 and (CuPt)50Ag0 samples are also visible.

ORR catalytic performance of the NPs/C catalysts, *i.e.*, onset potentials and average electron transfer numbers (n) (Table 3), was estimated from CV (Fig. 8a and b) and LSV results at different rotation speeds and K–L plots (Fig. 8c and Fig. S8, Table S1, ESI†). The results were compared with those of the commercial Pt/C reference catalyst. The onset potentials of the catalysts decrease in the order of Pt/C reference > Ag50Pt50 > Pt50 > (CuPt)50Ag30 > (CuPt)50Ag0. In addition, the electron transfer numbers decrease in the order of Pt/C reference > Pt50 > Ag50Pt50 > (CuPt)50Ag30 > (CuPt)50Ag0.

Overall, our sputtered NP catalysts performed worse than the Pt/C reference catalyst. Among all the synthesized samples, (CuPt)50Ag0/C is the worst with the smallest onset potential and electron transfer number. Below 0.3 V in the CV curve of (CuPt)50Ag0, Cu reduction occurs (Fig. 8b). This indicates Cu in the (CuPt)50Ag0/C catalyst was oxidized and possibly contributed to its poor catalytic performance. Moreover, the dispersions of (CuPt)50Ag0 NPs on carbon significantly changed before and after electrochemical tests (Fig. S9, ESI†). Before the test (CuPt)50Ag0 NPs distributed evenly on carbon (Fig. S9a,
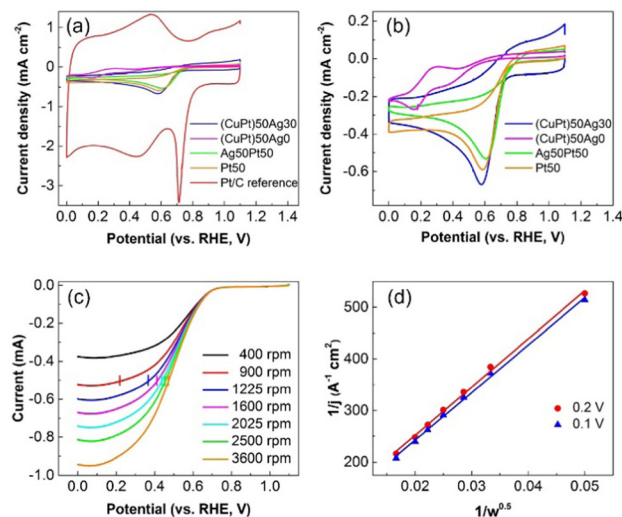
ESI†). However, after the test, although few NPs remain dispersed, most NPs aggregated (Fig. S9b and c, ESI†). Furthermore, after electrochemical tests the STEM-EDS area analysis of the catalyst indicates that there is almost no Pt and only a small amount of Cu (Fig. S10, ESI†). This means Pt and Cu dissolved in the electrolyte during the electrochemical tests. Previous reports also show that both Pt and the non-noble metal of Pt-based alloys dissolved into the electrolyte.[59,60] In our case, the amount of Cu in the catalysts is twice that of Pt (Table 2). This explains the observation that after dissolution of Cu and Pt, some Cu remained on the electrode whereas a small amount of Pt could not be measured by EDS area analysis. The dissolution of Pt and Cu also contributed to the low catalytic performance of the (CuPt)50Ag0/C catalyst.

Trimetallic alloy (CuPt)50Ag30/C catalyst containing Ag outperformed the bimetallic alloy (CuPt)50Ag0/C one. It is noted that the Cu : Pt molar ratio of the latter is higher than that of the former one (Table 4), suggesting more severe oxidation of Cu in the latter catalyst. Good dispersion of the trimetallic alloy NPs on the carbon support and both Cu and Ag present in the trimetallic alloy NPs before and after ORR catalytic tests were confirmed in STEM-HAADF images and EDS line profiles (Fig. S11–S13, ESI†). The trimetallic structure still existed in the NPs, and no significant shape or structure change was found, indicating that the NPs remained intact. This suggests that (CuPt)50Ag30 NPs have good composition and structure durability during the ORR measurement, and alloying of CuPt with Ag improves the stability and performance of the catalyst compared with (CuPt)50Ag0/C.

Regarding the onset potential, the sputtered Ag50Pt50 has a higher onset potential (0.74 V) than that of sputtered Pt50 (0.72 V) and (CuPt)50Ag30 (0.71 V). It is significant that although that Ag50Pt50 NPs contain 40 atom% Ag (Table 4),

Table 3 Electrochemical test results of the sputtered samples

Sample	(CuPt)50Ag30	(CuPt)50Ag0	Pt50Ag50	Pt50	Pt ref.
ORR onset potential (V)	0.71	0.58	0.74	0.72	0.77
Average electron transfer number, n	2.9	—	3.3	3.6	4.0

Table 4 Metal loading on the carbon support of the catalysts before the ORR from ICP results and Pt mass activity

Catalyst sample	Metal loading on carbon (wt%)			Cu : Pt (mol mol^{-1})	Ag : Pt (mol mol^{-1})
	Cu	Pt	Ag		
(CuPt)50Ag30/C	0.121	0.138	0.095	2.69 : 1	1.24 : 1
(CuPt)50Ag0/C	0.123	0.0661	—	5.71 : 1	0
Ag50Pt50/C	—	0.682	0.246	0	0.65 : 1
Pt50/C	—	0.337	—	0	0
Pt/C reference	—	5	—	0	0

they outperform Pt50 NPs. It has been reported that the geometric (*e.g.*, Pt–Pt interatomic distances) and electronic parameters influence the catalyst's ORR activity *via* varying the adsorption of Pt with O$_2$ and the intermediate oxygenated species and suitable interaction is needed for enhanced catalytic performance.[61,62] These two factors can be present in our catalyst and can be considered in discussion of the obtained results. In our previous work,[13] the sputtered Ag/Pt alloy NPs were found to have Pt 4f binding energy positively shifted and Ag 3d binding energy negatively shifted, according to the XPS results. This suggests the change of electronic structure of Pt by alloying with Ag with an increase of electron deficiency (*e.g.* Pt 5d-band vacancy), which is also reported by Feng *et al.*[61] Pure and/or small Pt NPs adsorb O$_2$ too strongly. Increased Pt electron deficiency would reduce electron back-donation from the Pt 5d-orbital to the adsorbed O$_2$, resulting in a weaker Pt–O interaction.[61] Appropriate weakening of Pt–O interaction can help improve the Pt activity toward the ORR.[61,62] Hence, the modification of the electronic structure of Pt and Ag *via* alloying can improve ORR performance of the Pt50Ag50 catalysts. In addition to the electronic effect caused by alloying, geometric effects, that is, a tensile strain of the lattice causes the d-band center of Pt to shift up, can affect the catalytic activity.[61,62] Since the lattice spacing of Ag is larger than that of Pt, the mismatch between Pt and Ag would lead to expansion of Pt lattice spacing with tensile strain, thus resulting in an upshift of the d-band center.[61] This upshift of the Pt d-band center would strengthen the binding of the oxygenated intermediates. This can decrease ORR activity by lowering the surface coverage.[61,62] However, it should be noted that both d-band downshift and d-band upshift to improve ORR catalytic activity have been suggested by researches[61,62] and the overall impact of the electronic structure modification of Pt and geometric effect by alloying on ORR activity remains a matter of debate. Possibly, the net impact of the electronic structure, geometric effect, particle size, and structural stability in Ag50Pt50 alloy NPs make them activate the ORR better than Pt in term of the overpotential. In addition, in order to obtain more detailed information, sample Ag50Pt50/C was chosen to for XPS measurements because of the highest metal loading on the carbon supports and its relatively higher catalytic activity among all the samples. The XPS results are shown in Fig. S14 (ESI†). The Pt 4f and Ag 3d peaks can be seen in the XPS spectra of the sample before electrochemical tests. The spin–orbit splitting of the Pt 4f peaks

are 3.3 eV (Pt 4f$_{5/2}$ at 74.2 eV and Pt 4f$_{7/2}$ at 70.9 eV), which is the characteristic of Pt. The XPS spectrum of Pt 4f after the electrochemical test was observed with similar intensity and peak position to that before the test. This indicates the chemical state of Pt is likely unchanged. However, the Ag 3d peaks after electrochemical tests were broad with low intensity compared with that before the test. This indicates that the Ag content is relatively lower. The Ag/Pt ratio of the sample after the electrochemical test measured by ICP is 0.33 : 1 (mol mol^{-1}), smaller than that of the catalyst before the experiments (0.65 : 1 (mol mol^{-1})). The result is consistent with XPS results, suggesting that Ag was possibly dissolved in the electrolyte during the electrochemical tests. This may also account for the reason why sample Ag50Pt50/C performs worse than Pt50/C. (CuPt)50Ag30 NPs are also alloys, however, the onset potential is lower than that of Ag50Pt50. For one thing, the average particle size of (CuPt)50Ag30 NPs (1.6 nm) is smaller than that of Ag50Pt50 (1.8 nm), making them less active catalyst in the ORR; for another, the Cu oxidation in (CuPt)50Ag30 NPs also reduces their catalytic properties.

The electron transfer numbers (*n*) of (CuPt)50Ag30/C, Ag50Pt50/C, and Pt50/C are 2.9, 3.3 and 3.6, respectively, are lower than that of commercial reference Pt (4.0). One possible reason is that the particle sizes of our sputtered samples (<2 nm) are smaller than that of the Pt/C reference catalyst (3.5 nm, Fig. S15, ESI†). It has been reported that Pt NPs with diameter of 3 nm have the optimized catalytic performances, because the NPs with this size have a maximum mass activity.[1,63] The active sites for the ORR of Pt NPs below 3 nm located on the terrace sites of the NPs decreases with particle size. Thus, decrease of particle size will decrease catalytic activity.[63] The average particle sizes of synthesized NPs are smaller than 2 nm whereas that of Pt reference is 3.5 nm. The size of Pt reference is closer to the ideal particle size for optimal ORR catalytic activity. For the sputtered NPs, the average size of sample (CuPt)50Ag30 is 1.6 nm (Table 1), and the average sizes of Pt50 and Ag50Pt50 are 1.6 and 1.8 nm,[13] respectively. But electron transfer number of the Ag50Pt50 sample (*n* = 3.3) is lower than that of Pt50 (*n* = 3.6). Further research is essential to shed light on these aspects for better understanding. One possibility is that geometric effects is more significant than the electronic effect caused by alloying of Pt with Ag, reducing the ORR in the 4-electron pathway. Moreover, the Pt compositions of the NPs decrease in the order of Pt50 > Ag50Pt50 > (CuPt)50Ag30. The NPs with higher Pt compositions, that is, more Pt nearby another Pt for simultaneous activation of two O, help enable the 4-electron pathway.[61] This may account for the fact that the electron transfer numbers of alloy NPs ((CuPt)50Ag30 and Ag50Pt50) are smaller than that of Pt50 NPs, and that of (CuPt)50Ag30 is smaller than that of Ag50Pt50. The oxidation of Cu in (CuPt)50Ag30 also leads to its smaller *n* compared to Pt50. The *n* values of the sputtered samples are between 2 and 4, which means during the electrochemical tests, two-electron and four-electron ORR occurred at the same time. However, the occurrence of Cu reduction reaction could reduce the calculated electron transfer number. Cu dissolved in

the acidic electrolyte and the Cu oxides of sample (CuPt)50Ag30 were reduced during the ORR possibly skewing the electron transfer number towards 2. The best (Pt50Ag50) and the worst ((CuPt)50) performing catalysts in acid electrolyte were chosen to measure catalytic performance in 1 M KOH electrolyte. The results are shown in Fig. S16 (ESI†). (CuPt)50Ag0 didn't dissolve in KOH, however, the onset potential (0.84 V) and electron transfer ($n = 3.5$) number of (CuPt)50Ag0 are still lower than that of Pt50Ag50 (0.88 V, $n = 3.6$).

So far, the detail mechanism of the ORR catalytic activity of the Ag/Pt alloy and CuPt/Ag NPs in our study is complicated, which is the topic for future study to address the contribution of electronic and geometrical structures, particle dispersion, alloy structure stability, and particle sizes on the catalytic performance.

Conclusions

Trimetallic CuPt/Ag alloy NPs were synthesized by co-sputtering onto liquid PEG using the CuPt alloy target and Ag target. The Ag compositions of NPs increase as the sputtering currents applied to the Ag target increase while the Cu : Pt molar ratios of NPs are lower than that of the CuPt alloy target. This is because the NPs with higher Cu compositions are too small to be detected by STEM-EDS area analysis, or some sputtered Cu atoms did not alloy with Ag and Pt. Thus the analyzed NPs that are bigger than 0.8 nm have lower Cu compositions. The trimetallic (CuPt)50Ag30 alloy NPs, bimetallic (CuPt)50Ag0 and Ag50Pt50 NPs, and Pt50 NPs were evaluated as ORR catalysts. Better catalytic activities of trimetallic (CuPt)50Ag30 NPs compared with bimetallic (CuPt)50Ag0 NPs came from better dispersion of the trimetallic NPs in the carbon support and a more stable alloying structure. However, bimetallic (CuPt)50Ag0 and trimetallic (CuPt)50Ag30 NPs performed worse than Pt50 and Ag50Pt50 NPs because of Cu oxidation. The synergy between Pt and Ag in the Ag50Pt50 alloy NPs is thought to enhance the catalytic properties of the bimetallic alloy NPs compared with only Pt NPs.

Author contributions

M. Z., M. T. N., and W. J. S. conducted the experiments and collected and analyzed the data. M. T. N. and T. Y. conceived the concept, designed the experiments, and supervised the project. M. Z. wrote the original draft. M. T. N. and T. Y. revised and edited the draft. All authors proofed the draft.

Conflicts of interest

There is no conflict of interest to declare.

Acknowledgements

References

1 I. Y. Cha, M. Ahn, S. J. Yoo and Y. Sung, *RSC Adv.*, 2014, **4**, 38575–38580.

2 B. R. Cuenya, *Thin Solid Films*, 2010, **518**, 3127–3150.

3 D. Du, Q. Geng, L. Ma, S. Ren, J. Li, W. Dong, Q. Hua, L. Fan, R. Shao, X. Wang, C. Li and Y. Yamauchi, *Chem. Sci.*, 2022, **13**, 3819–3825.

4 C. Li, M. Lqbal, J. Lin, X. Luo, B. Jiang, V. Malgras, K. C. Wu, J. Kim and Y. Yamauchi, *Acc. Chem. Res.*, 2018, **51**, 1764–1773.

5 C. Li, H. Tan, J. Lin, X. Luo, S. Wang, J. You, Y. Kang, Y. Bando, Y. Yamauchi and J. Kim, *Nanotoday*, 2018, **21**, 91–105.

6 C. Li, B. Jiang, N. Miyamoto, J. H. Kim, V. Malgras and Y. Yamauchi, *J. Am. Chem. Soc.*, 2015, **137**, 11558–11561.

7 C. Li, M. Lqbal, B. Jiang, Z. Wang, J. Kim, A. K. Nanjundan, A. E. Whitten, K. Wood and Y. Yamauchi, *Chem. Sci.*, 2019, **10**, 4054–4061.

8 J. Li, H. Yin, Q. Geng, D. Du, L. Ma, L. Fan, Q. Hua and C. Li, *J. Mater. Chem. A*, 2022, **10**, 6569–6575.

9 P. Song, H. Xu, B. Yan, J. Wang, F. Gao, Y. Zhang, Y. Shiraishi and Y. Du, *Inorg. Chem. Front.*, 2018, **5**, 1174–1179.

10 G. Zhang, Z. Yang, W. Zhang, H. Hu, C. Wang, C. Huang and Y. Wang, *Nanoscale*, 2016, **8**, 3075–3084.

11 L. Zheng, D. Yang, R. Chang, C. Wang, G. Zhang and S. Sun, *Nanoscale*, 2017, **9**, 8918–8924.

12 Z. Li, Y. Li, C. He and P. K. Shen, *J. Mater. Chem. A*, 2017, **5**, 23158–23169.

13 M. Zhu, M. T. Nguyen, Y. R. Chau, L. Deng and T. Yonezawa, *Langmuir*, 2021, **37**, 6096–6105.

14 P. J. Kelly and R. D. Arnell, *Vacuum*, 2000, **56**, 159–172.

15 H. Wender, P. Migowski, A. F. Feil, S. R. Teixeira and J. Dupont, *Coord. Chem. Rev.*, 2013, **257**, 2468–2483.

16 G. Bräuer, B. Szyszka, M. Vergöhl and R. Bandorf, *Vacuum*, 2010, **84**, 1354–1359.

17 O. K. Alexeeva and V. N. Fateev, *Int. J. Hydrogen Energy*, 2016, **41**, 3373–3386.

18 M. T. Nguyen and T. Yonezawa, *Sci. Technol. Adv. Mater.*, 2018, **19**, 883–898.

19 M. Wagener and B. Günther, *J. Magn. Magn. Mater.*, 1999, **201**, 41–44.

20 T. Torimoto, K. Okazaki, T. Kiyama, K. Hirahara, N. Tanaka and S. Kuwabata, *Appl. Phys. Lett.*, 2006, **89**, 243117.

21 Y. Oda, K. Hirano, K. Yoshii, S. Kuwabata, T. Torimoto and M. Miura, *Chem. Lett.*, 2010, **39**, 1069–1071.

22 S. C. Hamm, R. Shankaran, V. Korampally, S. Bok, S. Praharaj, G. A. Baker, D. Robertson, B. D. Lee, S. Sengupta, K. Gangopadhyay and S. Gangopadhyay, *ACS Appl. Mater. Interfaces*, 2012, **4**, 178–184.

23 K. Yoshii, K. Yamaji, T. Tsuda, H. Matsumoto, T. Sato, R. Izumi, T. Torimoto and S. Kuwabata, *J. Mater. Chem. A*, 2016, **4**, 12152–12157.

24 K. Okazaki, T. Kiyama, K. Hirahara, N. Tanaka, S. Kuwabata and T. Torimoto, *Chem. Commun.*, 2008, 691–693.

25 H. Wender, L. F. de Oliveira, A. F. Feil, E. Lissner, P. Mingowski, M. R. Meneghetti, S. R. Teixeira and J. Dupont, *Chem. Commun.*, 2010, **46**, 7019–7021.

26 Y. Hatakeyama, T. Morita, S. Takahashi, K. Onishi and K. Nishikawa, *J. Phys. Chem. C*, 2011, **115**, 3279–3285.

27 M. T. Nguyen, L. Deng and T. Yonezawa, *Soft Matter*, 2022, **18**, 19–47.

28 Y. Ishida, A. Morita, T. Tokunaga and T. Yonezawa, *Langmuir*, 2018, **34**, 4024–4030.

29 Y. Ishida, R. Nakabayashi, R. D. Corpuz and T. Yonezawa, *Colloids Surf., A*, 2017, **518**, 25–29.

30 M. Porta, M. T. Nguyen, T. Tokunaga, Y. Ishida, W.-R. Liu and T. Yonezawa, *Langmuir*, 2016, **32**, 12159–12165.

31 Y. Ishida, I. Akita, T. Sumi, M. Matsubara and T. Yonezawa, *Sci. Rep.*, 2016, **6**, 29928.

32 Y. Ishida, R. D. Corpuz and T. Yonezawa, *Acc. Chem. Res.*, 2017, **50**, 2986–2995.

33 S. Suzuki, T. Suzuki, Y. Tomita, M. Hirano, K. Okazaki, S. Kuwabata and T. Torimoto, *CrystEngComm*, 2012, **14**, 4922–4926.

34 M. Hirano, K. Enokida, K. Okazaki, S. Kuwabata, H. Yoshida and T. Torimoto, *Phys. Chem. Chem. Phys.*, 2013, **15**, 7286–7294.

35 D. König, K. Richter, A. Siegel, A. Mudring and A. Ludwig, *Adv. Funct. Mater.*, 2014, **24**, 2049–2056.

36 M. T. Nguyen, T. Yonezawa, Y. Wang and T. Tokunaga, *Mater. Lett.*, 2016, **171**, 75–78.

37 A. Chauvin, A. Sergievskaya, A. E. Mel, A. Fucikova, C. A. Corrêa, J. Vesely, E. Duverger-Nédellec, D. Cornil, J. Cornil, P. Tessier, M. Dopita and S. Konstantinidis, *Nanotechnology*, 2020, **31**, 455303.

38 L. Deng, M. T. Nguyen, J. Shi, Y. R. Chau, T. Tokunaga, M. Kudo, S. Matsumura, N. Hashimoto and T. Yonezawa, *Langmuir*, 2020, **36**, 3004–3015.

39 L. Deng, M. T. Nguyen, S. Mei, T. Tokunaga, M. Kudo, M. Matsumura and T. Yonezawa, *Langmuir*, 2019, **35**, 8418–8427.

40 M. T. Nguyen, H. Zhang, L. Deng, T. Tokunaga and T. Yonezawa, *Langmuir*, 2017, **33**, 12389–12397.

41 Y. R. Chau, M. T. Nguyen, M. Zhu, A. Romier, T. Tokunaga and T. Yonezawa, *New J. Chem.*, 2020, **44**, 4704–4712.

42 X. Cai, C. Liu, Y. Lu, Y. Zhong, K. Nie, J. Xu, X. Gao, X. Sun and S. Wang, *Nano-Micro Lett.*, 2017, **9**, 48.

43 F. Kong, Z. Ren, M. N. Banis, L. Du, X. Zhou, G. Chen, L. Zhang, J. Li, S. Wang, M. Li, K. Doyle-Davis, Y. Ma, R. Li, A. Young, M. Markiewicz, Y. Tong, G. Yin, C. Du, J. Luo and X. Sun, *ACS Catal.*, 2020, **10**, 4205–4214.

44 H. A. Gasteiger, S. S. Kocha, B. Sompalli and F. T. Wagner, *Appl. Catal., B*, 2005, **56**, 9–35.

45 A. U. Nilekar, Y. Xu, J. Zhang, M. B. Vukmirovic, K. Sasaki, R. R. Adzic and M. Mavrikakis, *Topics Catal.*, 2007, **46**, 276–284.

46 J. Luo, P. N. Njoki, Y. Lin, L. Wang and C. J. Zhong, *Electrochem. Commun.*, 2006, **8**, 581–587.

47 C. Gümeci, Z. R. Li, D. J. Casadonte Jr. and C. Korzeniewski, *J. Electrochem. Soc.*, 2012, **159**, F35–F41.

48 C. Wang, M. Chi, G. Wang, D. van der Vliet, D. Li, K. More, H.-H. Wang, J. A. Schlueter, N. M. Markovic and V. R. Stamenkovic, *Adv. Funct. Mater.*, 2011, **21**, 147–152.

49 J. Sha, S. Paul, F. Dumeignil and R. Wojcieszak, *RSC Adv.*, 2019, **9**, 29888–29901.

50 M. Liu, F. Chi, J. Liu and F. Wang, *RSC Adv.*, 2016, **6**, 62327–62335.

51 N. Toshima and T. Yonezawa, *New J. Chem.*, 1998, **22**, 1179–1201.

52 F. H. Lima, C. D. Sanches and E. A. Ticianelli, *J. Electrochem. Soc.*, 2005, **152**, A1466–A1473.

53 H. Liu, F. Ye, Q. Yao, H. Cao, J. Xie, J. Y. Lee and J. Yang, *Sci. Rep.*, 2014, **4**, 3969.

54 R. C. Sekol, X. Li, P. Cohen, G. Doubek, M. Carmo and A. D. Taylor, *Appl. Catal., B*, 2013, **138**, 285–293.

55 F. Qu, N. B. Li and H. Q. Luo, *J. Phys. Chem. C*, 2013, **117**, 3548–3555.

56 A. Campos, N. Troc, E. Cottancin, M. Pellarin, H. Weissker, J. Lermé, M. Kociak and M. Hillenkamp, *Nature Phys.*, 2019, **15**, 275–280.

57 S. Baset, H. Akbari, H. Zeynali and M. Shafie, *Dig. J. Nanomater. Biostruct.*, 2011, **6**, 709–716.

58 D. Nafday, S. Sarkar, P. Ayyub and T. Saha-Dasgupta, *ACS Nano*, 2018, **12**, 7246–7252.

59 H. R. Colón-Mercado and B. N. Popov, *J. Power Sources*, 2006, **155**, 253–263.

60 M. Watanabe, K. Tsurumi, T. Mizukami, T. Nakamura and P. Stonehart, *J. Electrochem. Soc.*, 1994, **141**, 2659–2668.

61 Y. Feng, G. Zhang, J. Ma, G. Liu and B. Xu, *Phys. Chem. Chem. Phys.*, 2011, **13**, 3863–3872.

62 F. Ando, T. Gunji, T. Tanabe, I. Fukano, H. D. Abruña, J. Wu, T. Ohsaka and F. Matsumoto, *ACS Catal.*, 2021, **11**, 9317–9332.

63 F. J. Perez-Alonso, D. N. McCarthy, A. Nierhoff, P. Hernandez-Fernandez, C. Strebel, I. E. L. Stephens, J. H. Nielsen and I. Chorkendorff, *Angew. Chem., Int. Ed.*, 2012, **51**, 4641–4643.